Wide-Frequency-Range Dielectric Tuning of BaTiO3 by Embedding Metal Nanocrystals

Deli SHI
Southwest University of Science and Technology
Leiming FANG
China Academy of Engineering Physics Institute of Nuclear Physics and Chemistry
Xiaoqiang Zhang
China Academy of Engineering Physics Institute of Electronic Engineering
Jinlong TANG
Southwest University of Science and Technology
Jun LI
China Academy of Engineering Physics Institute of Fluid Physics
Yajun FU
Southwest University of Science and Technology
Jin WANG
southwest university of science and technology
Zhipeng GAO
China Academy of Engineering Physics Institute of Fluid Physics
Zhengwei XIONG (zw-xiong@swust.edu.cn)
southwest university of science and technology

Research Article

Keywords: Dielectric, Capacitor, Nanocrystals, Epitaxial

Posted Date: November 3rd, 2020

DOI: https://doi.org/10.21203/rs.3.rs-99563/v1

Wide-frequency-range dielectric tuning of $BaTiO_3$ by embedding metal nanocrystals

Deli SHI[1], Leiming FANG[2], Xiaoqiang ZHANG[3], Jinlong TANG[1†], Jun LI[4], Yajun FU[1], Jin WANG[1], Zhipeng GAO[1,4], Zhengwei XIONG[1†]

Affiliations:

[1]Joint Laboratory for Extreme Conditions Matter Properties, Southwest University of Science and Technology, Mianyang, 621010, China

[2]Institute of Physics Nuclear and Chemistry, China Academy of Engineering Physics, Mianyang, 621900, China

[3] Institute of Electronic Engineering, China Academy of Engineering Physics, Mianyang, Mianyang, 621900, China

[4]Institute of Fluid Physics, China Academy of Engineering Physics, Mianyang, 621900, China

*Corresponding author:

Jinlong Tang (jl.tang@foxmail.com)

Zhengwei Xiong (zw-xiong@swust.edu.cn)

* Project supported by National Natural Science Foundation of China (Grant No. 11904299, 11704353, U1930124, 11804312), Scientific Reserch Fund of SiChuan Provincial Education Department (18ZA0503 and 17ZA0406) and CAEP Foundation (2018AB02).
† Corresponding author. E-mail: jl.tang@foxmail.com
† Corresponding author. E-mail: zw-xiong@swust.edu.cn.

Abstract

The Fe nanocrystals (NCs) were embedded into the epitaxial $BaTiO_3$ (BTO) matrix. According to optimize growth processes, a novel nanocomposite system was constructed, which consist of well epitaxial BTO layer and three-dimensional Fe NCs. Based on this, the different dielectric response in the regions of low temperature-high frequency and low frequency-high temperature were revealed by the contribution of hopping and interfacial polarizations, respectively. With the increased amount of Fe NCs, the obvious enhancement of low-frequency conductivity, middle frequency capacitance and high-frequency inductive effect was found. The metal NC embedding plays an important role in tuning the dielectric behaviors and ac conductivity of oxide dielectrics. This significant rectification effect in the wide-frequency ranges opens up a new direction for the designing of embedded nano-capacitors.

Keywords: Dielectric, Capacitor, Nanocrystals, Epitaxial

1. Introduction

Ceramic-metal composites (CMCs), a classical giant dielectric material composed of metal particles and dielectric ceramics, has a wide application in the high sensitive sensors, thin-layer capacitors, gate dielectrics and so on.[1-10] In the CMCs model, the ceramics matrix function the insulating phase while the metal particles are used as the conductive fillers.[4-10] The enhanced permittivity of CMCs system is mainly assigned to the interfacial polarization induced by the increased interfaces between conductive metal particles and insulating ceramics. Compared with other dielectric composites, CMCs system performs two merits: (1) the enhanced giant permittivity is mainly relative to the metal particles rather than the dielectric matrix; (2) dielectric properties of the CMCs could be adjusted by changing the composition/configuration.[11-22] Consequently, there have been numerous dielectric investigations focused on the CMCs. The increased permittivity of $SrTiO_3$ was up to 2150 with the Pt addition.[23] Besides, adding Ni or Ag nanoparticles into BTO ceramic could both attain the superior dielectric properties. [1, 24] The colossal dielectric response of CMCs has been successfully elaborated by the percolation theory, revealing that the colossal permittivity was controlled by a critical content of the metal particles.

In addition, the metal particles and the ceramic in the CMCs also could be regard as the conductive electrodes and insulating dielectric, which could be further equivalent to a series of embedded capacitors. So, the CMCs system could be simplified as a circuit model, consisting of capacitor, resister and inductance components. As we all know, the three circuit elements are closely linked with the frequencies.[25] Unfortunately, the contribution of capacitor, resister and inductance effect to the dielectric behaviors of CMCs at varied

frequencies was not clarified in the percolation theory.

In this work, we embedded the Fe NCs into BTO dielectric matrix, and achieved a co-existence system contained NCs and epitaxial dielectric matrix. Compared with other typical polycrystalline ceramics in CMCs, the well epitaxial BTO matrix almost exhibited no grains and grain boundaries,[26] providing an ideal mode to disclose and analyze the electric mechanism induced by the metal NCs at wide frequency regions. The dielectric properties and ac conductivity in the Fe NCs-BTO composites were investigated in the wide frequency ranges from 0.1 to 10^7 Hz. Based on this, the influence of capacitor, resister and inductance in the CMCs was explained clearly.

2. Experimental

The Fe NCs-BTO composites were grown by L-MBE technology. The KrF excimer laser (248 nm wavelength) with laser energy density 3 J/cm^2 and frequency of 2 Hz was alternately used to ablate the commercial single crystal targets of BTO and Fe (purity > 99.99%). The epitaxial films consisting of Fe NCs and BTO was prepared on the (001) $SrTiO_3$ substrate ($10\times5\times0.5$ mm^3). The deposition pressure of film growth process is in an ultra-high-vacuum chamber at 5×10^{-6} Pa. The ablated material was collected on the $SrTiO_3$ substrate located at a distance of 5 cm from the targets. Firstly, a homo-epitaxy BTO buffer layer was grown on the substrate. As a reference, the epitaxial BTO thin films were set as a same thickness in the varied Fe NCs-BTO samples. After each BTO layer, oxygen gas was introduced into the chamber to offer a background pressure of 10 Pa for annealing 20 min. Then the Fe NCs were deposited at 200, 500 and 800 laser pulses (signed as P1, P2 and P3, respectively). Next, a uniform thickness BTO layer with was recovered on the Fe NCs subsequently. After that, the

Fe NCs/BTO cycle was repeated.

The deposition and growth progress of the films were measured *in-situ* using a reflection high-energy electron diffraction (RHEED) system. The typical energy of the electron was 25 keV, and a CCD camera was used to observe the diffraction pattern, then analyzed the results with a commercial software. Atomic force microscopy (AFM) was utilized to observe the morphologies of Fe NCs-BTO nanocomposites and estimate the spacing (*R*) between the Fe NCs and the diameters (*D*) of Fe NCs by statistics. The dielectric properties of films were measured using an impedance analyzer (HP 4294A, Agilent) in the frequency range from 0.1 to 10^7 Hz. The Au top electrode (10×5 mm^2) was formed on fabricated composite films by the L-MBE. The 0.5 wt% Nb:$SrTiO_3$ (001) substrate (10×5 mm^2) was used as the bottom electrode.

3. Results and discussion

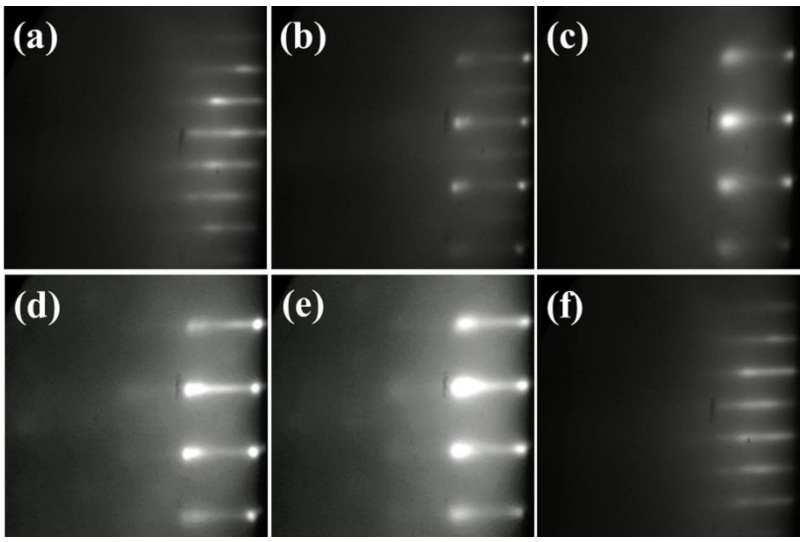

Fig. 1 Evolution of RHEED patterns during the Fe NCs-BTO composites growth at various time: (a) complete surface of BTO epitaxial film deposited on (001) $SrTiO_3$ substrates, and the Fe NCs deposition on BTO surface at (b) 50 s, (c) 100 s, (d) 250 s and (e) 400 s, (f) fresh surface of BTO grown on the Fe NCs.

Fig. 1 displays the RHEED monitoring results during the growth of the Fe NCs-BTO nanocomposites at varied laser pulses. Obviously, the RHEED patterns of the BTO surface deposited on (001) $SrTiO_3$ substrates are the remarkably streaky diffraction (see Fig. 1a), implying that the BTO exhibits a well two-dimensional (2D) layer-by-layer epitaxial growth and owns a much smooth surface. Then depositing Fe with different growth time on the BTO surface, we can observe that the RHEED patterns gradually become bright spots (see Fig. 1b-e), suggesting a rougher surface with increasing number of laser pulses acted on the Fe target. Here, the appearance of bright diffraction spots was derived from the high energy e-beam penetrating through the protrusions on the BTO surface [2, 3, 18]. This case can be also considered as the formation of three-dimensional (3D) islands, named NCs. Subsequently, a uniform thickness of BTO layer grows on the Fe NCs, and the diffraction images recover to the noticeable diffraction streaks, confirming the reappearance of the layer-by-layer mode of BTO epitaxial growth (Fig. 1f). This transition of growth mode from 2D layer-by-layer (BTO) to 3D island (Fe NCs) to 2D layer-by-layer (BTO) indicates that the embedded Fe NCs would not hinder the epitaxial growth of BTO matrix. As the formation of the 3D islands, the lattice mismatch between the Fe and BTO caused by strain energy would be released, which extremely reduces the effect of strained distortions and the interfacial stress is extremely reduced. The detail mechanism of lattice relaxation was revealed in our past works [2, 3, 18, 19]. Thus, we could artificially engineer such NCs growth in an epitaxial dielectric matrix. Compared with other polycrystalline matrix, the well epitaxial BTO layers in this Fe NCs-BTO system contains no grains and grain boundaries. Hence, the BTO film between the embedded NCs and contact interfaces between the NCs and BTO film can be

regard as the grains and grain boundaries, respectively. An ideal model is provided for explaining the effects of the interaction for NCs, grains and grain boundaries on its properties.

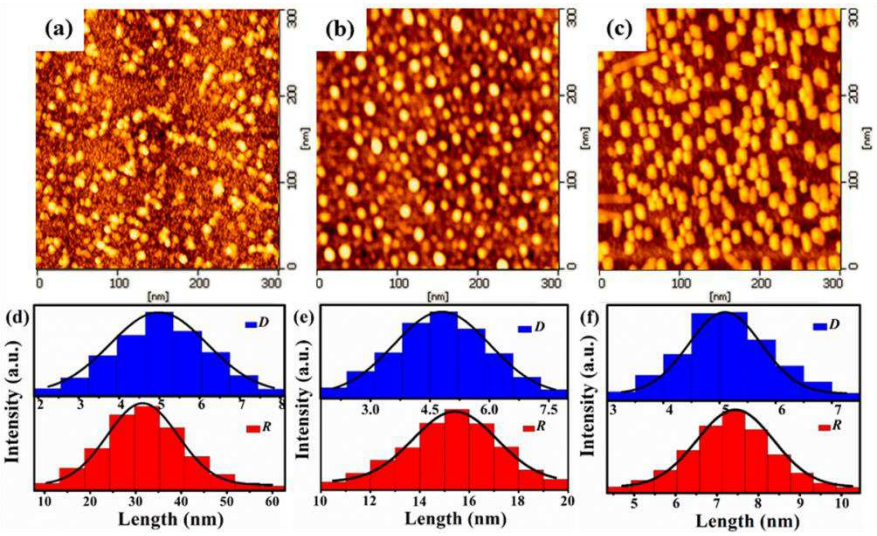

Fig. 2 AFM images of (a) P1, (b) P2 and (c) P3 sample; D and R distribution of Fe NCs fitted by a log-normal distribution of (d) P1, (e) P2 and (f) P3 sample, respectively.

As the AFM images shown of Fe NCs-BTO films in Fig. 2, many small NCs are sparsely distributed on the epitaxial BTO matrix, corresponding to the diffraction spots of REHHD results (Fig. 1b-e). With the increase of deposition time, denser Fe NCs are presented on the BTO surface, suggesting the obviously decreased *R* between the Fe NCs. To analysis the *D* and *R* of Fe NCs clearly, the average values of *D* and *R* is given in Fig. 2, corresponding to *D*=4.9, 5.0 and 5.2 nm and *R*=32.5, 15.6 and 7.8 nm for P1, P2 and P3 sample, respectively. So the spacing between the Fe NCs is gradually decreased while the NC diameters are almost unchanged with increasing amount of Fe NCs. This result means that the number of equivalent grains (the BTO films between NCs) and grain boundaries (contact interfaces between the NCs and BTO) increases as well.

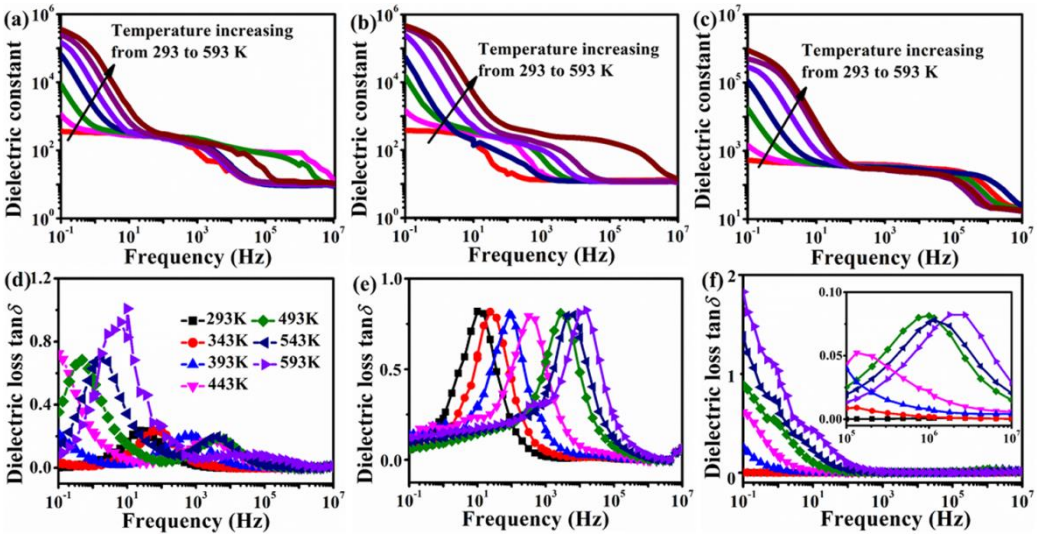

Fig. 3 Dielectric constant at varied temperature of (a) P1, (b) P2 and (c) P3 sample; dielectric loss tanδ of (d) P1, (e) P2 and (f) P3 at varied temperatures. The inset of (f) is the enlarged view pattern at high frequency.

As the real part of dielectric constant (ε') at varied temperature of all samples displayed in Fig. 3, the ε' plots of Fe NCs-BTO thin films possess the following features: (1) as the increased values of temperature from 293 to 593 K, the ε' rises rapidly and a strong dispersion is also observed at low frequency (<100 Hz), which can be attributed to the increased microscopic interfacial electron charge density activated by increasing temperature [1, 6, 12, 13, 18]; (2) with the decreased R, the values of ε' are also increased; (3) a frequency dependent ε' in the low and high frequency regions can be observed while a frequency independent plateau is presented in midfrequency regions. The abnormal ε' at low and high frequencies could be explained by the MW function and Debye law, respectively [12, 13, 18, 20]. Generally, the resultant low-frequency ε' of dielectric materials is due to different types of polarization (dipolar, ionic, electronic and interfacial) [21]. Electronic and ionic relaxations are related to very rapid oscillations of weak dipoles, and are only measurable at high frequencies (>10^{10}

Hz) [21]. Dipolar and interfacial polarization are usually contributed to the colossal permittivity at low frequencies [18, 21]. Many researchers have reported that the origin of colossal ε' in BTO composites ceramics was the result of the hopping polarization within grains and the interfacial polarization at the grain boundaries [6, 18, 21]. In this work, increasing the embedded amount of Fe NCs and resultantly decreasing spacing R between the NCs can correspond to the changes of equivalent grains and grain boundaries, which should be also contributed to the abnormal dielectric response. To further clarify the effect of grains and grain boundaries on the dielectric property for varied samples, the contributions of the hopping polarization and interfacial polarization to the ε' in the Fe NCs-BTO composites will be quantitatively analyzed later.

As the dielectric loss (tanδ) of P1 shown in Fig. 3, an obvious tanδ peak appeared at low frequency while a weaker peak is displayed in midfrequency region (Fig. 3d). With the increased amount of Fe NCs for P2 sample (Fig. 3e), low-frequency peak in the P1 is quenching, and only one tanδ peak is prominently emerged at midfrequency. Further increasing Fe NCs amount induces the disappearance of midfrequency peak in P2 and produce a weak peak at high frequency in P3 (Fig. 3f). These resonant frequency (f) peaks would move to high frequency as the increase of temperature for all samples. The shifting of dielectric loss peaks is well correlated with the variation of dielectric constants. In combination with the ε' and tanδ, the dielectric relaxation is gradually weakened and moved from low frequency to high frequency with the increase of Fe NCs amount.

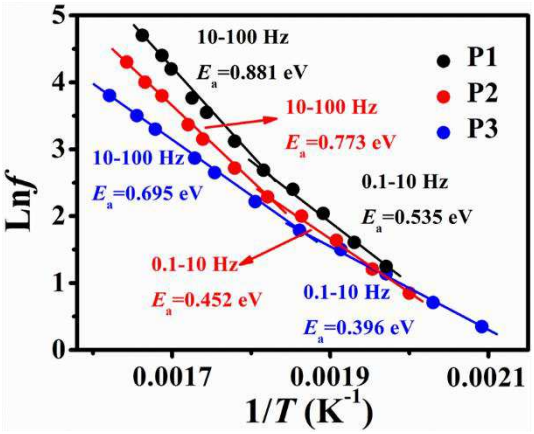

Fig. 4 Activation energy of thermally activated relaxations for the samples.

As we all known, the relaxation frequency can be represented by:

$$f = f_0 \exp(-E_a/k_B T) \quad (1)$$

where f_0, E_a, k_B and T is the characteristic relaxation frequency at infinite temperature, activation energy for relaxation, Boltzmann's constant and temperature, respectively. The imaginary part of dielectric constant (ε'') is proportional to $f\tau/(1+f\tau)^2$, and the maxima value of ε'' occurs under the condition $f\tau$=1, where τ is the dielectric relaxation time. Therefore, the relaxation temperature at different frequency can be extracted from the maximums of ε'', and E_a can be estimated further, where the E_a of varied samples estimated by Arrhenius plots is shown in Fig. 4. Two different slopes of the fitted curves for the Fe NCs-BTO are observed, suggesting the existence of two different thermally activated polarization mechanisms [6, 18]. One of E_a=0.535, 0.452 and 0.396 eV occurs at low temperature and higher frequency, while the other E_a=0.881, 0.773 and 0.695 eV are obtained at low frequency and high temperature for P1, P2 and P3 sample, respectively. Obviously, the E_a is decreasing with more Fe NCs, which can be assigned to local filed enhancement of NCs [18, 22]. For the Fe NCs-BTO composites, the smaller E_a at low temperature and high frequency indicates the hopping

polarization processes within grains (the BTO films between NCs), while the higher value of E_a at low frequency and high temperature implies interfacial polarization induced by the grain boundaries (the interfaces of Fe NCs and BTO) [6, 18]. Thus, the colossal permittivity can be attributed to the contributions of hopping polarization at low temperature and high frequency, and the interfacial polarization at low frequency and high temperature, respectively.

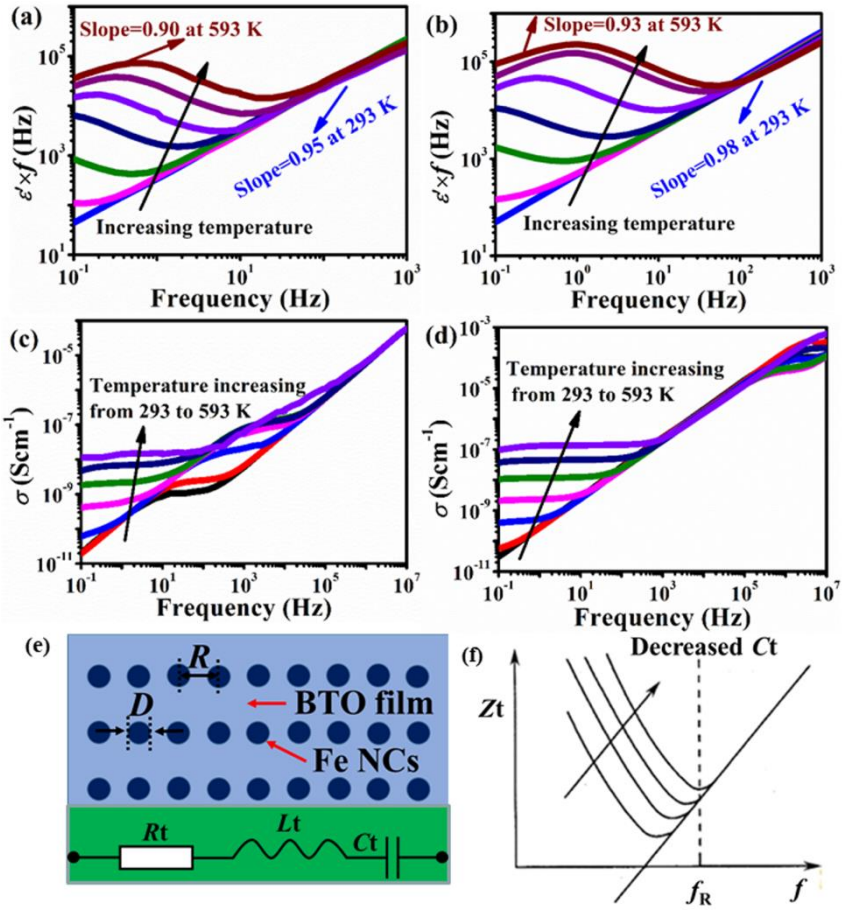

Fig. 5 Lg($\varepsilon' \times f$) vs lg$f$ plot of (a) P1 and (b) P3 sample at different temperatures; frequency dependence ac conductivity (σ) of varied samples at different temperature: (c) P1 and (d) P3, respectively; (e) schematic diagram and of Fe NCs-BTO composites, and the below inset displays the equivalent electric model of this system, where the Rt, Lt and Ct is the total resister, inductance and capacitance, respectively; (f) the frequency dependence total impedance (Zt) of RLC electric model.

To further prove this assumption clearly, the ε' in the universal dielectric response model can be written as follows:

$$f\varepsilon' = A(T)f^s \quad (2)$$

where $A(T)=\tan(s\pi/2)\sigma_0\varepsilon_0$, f, ε_0, σ_0 and s is the frequency, pre-exponential factor, permittivity of free space and the constant (0-1). Therefore, the slope of a straight line shown in $\lg(\varepsilon' \times f)$ vs $\lg f$ plot in Fig. 5 at a given temperature represents the value of s. The fitted straight line is deviated from the slope as frequency increases due to relaxation, and subsequently it decreases in a step-like behavior and displays another straight line at the high temperature region. Two different slopes are observed in all samples, which locate at low temperature-high frequency and high temperature-lower frequency, suggesting two different dominated polarizations [6, 18]. One of s=0.95 and 0.98 occurs at 293 K and higher frequency, while the other s=0.90 and 0.93 are obtained at 593 K and lower frequency for P1 and P3 sample, respectively. Actually, as the value of s is closer to 1, the polarization charges are more strictly localized [6, 18, 22]. Compared to high temperature-lower frequency region, the larger s at low temperature-higher frequency reveals the more localized charge carriers of polarization. It is obvious that more amounts of Fe NCs with stronger local filed enhancement induce the larger values of s. Due to the certain energy to overcome the relatively small energy barrier for polarization, the hopping polarization is becoming active at high frequency and low temperature. Nevertheless, the sufficient energy to overcome the large energy barrier at low frequency and high temperature is the interfacial polarization, which is associated with mobile electrons in the NCs and holes in the BTO are activated [18, 22]. Therefore, the hopping polarization play a primary role in the low temperature-higher

frequency while and the interfacial polarization is dominated at high temperature-lower frequency.

In the reported study, the colossal ε' has been attributed to MW-type contributions of the grains and insulating grain boundaries in the IBLCs model [23]. On the assumption of IBLCs model, the periodic Fe NCs-BTO nanostructure can be equivalent to a series connection of conductive Fe NCs and insulating BTO, where the NCs and the contact interfaces between Fe NCs and BTO plays the role of grains and grain boundaries, respectively. Based on the analysis, this structure is much similar with the IBLCs model. Thus, the contribution of interfacial polarization to the colossal permittivity at high temperature of 593 K and low frequency of 0.1 Hz can be calculated by using the IBLCs model [23], which can be presented by:

$$\varepsilon_{eff} = \varepsilon' D/R \tag{3}$$

where ε_{eff}, ε', D and R is the effective permittivity, real permittivity of the material, grain size and thickness of grain boundary, respectively. Taking the P1 as an example, the real permittivity of BTO is ε'=355410 at 0.1 Hz and 593 K. The measured D of varied samples are both ~5 nm, and the R is 32.5 nm for the P1. Thus, the effective permittivity of 125104 is calculated, which is equivalent to 15.4 % of the experimental colossal permittivity. Therefore, the colossal permittivity at high temperature and low frequency can be attributed to the 15.4 % interfacial polarization and 84.6% hopping polarization in the P1. Based on this estimation, the relative contribution of interfacial and hopping polarizations is calculated for each sample. The proportion of interfacial polarization is 15.4 %, 32.1% and 64.1%, while the hopping polarization is 84.6 %, 67.9% and 35.9% for the P1, P2 and P3 samples, respectively. As the

decreased R of Fe NCs, the interfacial polarization gradually plays a dominate role in the colossal dielectric response at high temperatures-lower frequency. Consequently, the interfacial and hopping polarization can be tuned quantitatively by adjusting the R between the Fe NCs in this nano-CMCs system.

As the σ-f curves of samples at different temperature displayed in Fig. 5, the σ values are increased with the increase of temperature, which agrees well with the reported dielectric ceramics [1, 6, 12, 13, 22, 23]. By contrast, the P1 and P3 possess the following differences: (1) at the low frequency, both the P1 and P3 have a frequency independence plateau, also named dc conductivity σ_0, while the plateau values of σ for P3 are higher than that of P1, which is due to the increased concentration of Fe NCs; (2) in the midfrequency region, the P1 owns a narrow plateau in this frequency range, while the σ of P3 becomes a linear correlation with frequencies; (3) at high frequency, the σ of P1 at varied temperature is dependent of frequency, while the P3 owns a narrow plateau. In the conventional jump relaxation model ($\sigma=\sigma_0+A_1\omega^{n1}+A_2\omega^{n2}$) [8], the lg$\sigma$-lg$f$ curves were increased linearly with different slopes in midfrequency and high frequency regions, differing with our results.

To clarify the variation discussed above, the typical RLC electric model is utilized in this system. As schematic diagram show in Fig. 5 (e), the embedded Fe NCs in the epitaxial BTO film and the spacing between the Fe NCs can be regard as the electrodes and spacing between the electrodes in a capacitor, respectively. In addition, the metal NCs owns an intrinsic resister and parasitic inductance [24]. Therefore, the Fe NCs-BTO system can be simplified as a typical RLC electric model (see the inset in Fig. 5e). Furthermore, the Zt in the RLC electric system is equal to Rt+$j\omega L$t-1/$j\omega C$t, where the ω is angular frequency ($\omega=2\pi f$).

In combination with the frequency dependence Zt of classical RLC model in Fig. 5 (f), it is clear that the resonant frequency (f_R) would move to high frequency with the decreased Ct [24].

Here, the narrow σ plateaus of P1 at midfrequency region can be assigned to the relaxation of dielectric constant (see Fig. 3a). With the decreased R of Fe NCs, Ct is increasing (Ct $=\varepsilon' S/R$, where S and R represents the area and spacing between Fe NC electrodes, respectively), meaning the enhanced capacitance effect (blocking dc current and flowing ac current). As a result, the ability of blocking dc current and flowing ac current is increased, which leads to the linear dependence of σ-f at midfrequency region for P3. Furthermore, at high frequency the narrow σ plateaus of P3 can be attributed to the NCs inductance effect (blocking high-frequency ac current and flowing high-frequency dc current). With the increased amount of Fe NCs, the Lt is increasing [24], implying the enhanced inductance effect. So the ability of blocking ac current and flowing dc current is increased, resulting in the plateaus of P3 at high frequency region relative to the linear dependence of σ-f in P1. Increasing the amount of Fe NCs induces the obvious enhancement of low-frequency conductivity, midfrequency capacitance effect and high-frequency inductive effect. Therefore, the NC embedding plays an important role in adjusting the ac conductivity in CMCs systems. The obvious rectification effect offers a well nano-CMCs system to the application in the dielectric capacitor and other electric devices.

4. Conclusions

In summary the Fe NCs were controllably embedded in epitaxial BTO matrix via L-MBE method. Compared with other polycrystalline matrix, the well epitaxial BTO layers in this Fe

NCs-BTO system contains no grains and grain boundaries. The BTO films between embedded NCs and the contact interfaces between the NCs and BTO film can be regard as the grains and grain boundaries, respectively. Further tuning the spacing between the NCs, the enhancement of colossal dielectric constant and shifting of dielectric loss peak from low to high frequencies were achieved. The abnormal dielectric responses could be explained by the quantitatively contribution of interfacial polarization and hopping polarization at various frequencies and temperatures. Based on the Fe NCs-BTO system, the effect of grains and grain boundaries to the colossal dielectric constant at low frequencies and high temperatures was clearly clarified. Significantly, decreasing the spacing between Fe NCs induces the obvious enhancement of low-frequency conductivity, midfrequency capacitance effect and high-frequency inductive effect. Such ideal model was provided for explaining the effects of the interaction for NCs, grains and grain boundaries on its dielectric and rectification characteristic. This new kind of nano-CMCs model opens up prospects for the application in aspect of embedded nano-capacitances.

Declaration of competing interest

The authors declare that they have no known competing financial interests or personal relationships that could have appeared to influence the work reported in this paper.

Acknowledgements

This work was supported by National Natural Science Foundation of China (Grant No. 11904299, 11704353, U1930124), Scientific Research Fund of Sichuan Provincial Education Department (Grant No. 18ZA0503) and CAEP Foundation (2018AB02).

References

[1] Luo B C, Wang X H, Tian E K, *et al*. Giant permittivity and low dielectric loss of Fe doped $BaTiO_3$ ceramics: experimental and first-principles calculations. *J Eur Ceram Soc* 2018, **38**:1562-1568.

[2] Shi D, Xiong Z, Li J, Luo B, *et al*. Electron transition and electron-hole recombination processes in epitaxial $BaTiO_3$ films with embedded Co nanocrystals. *Mater Res Express* 2019, **6**:105021.

[3] Gavalda Diaz O, Axinte D, Butler-Smith P, *et al*. On understanding the microstructure of SiC/SiC Ceramic Matrix Composites (CMCs) after a material removal process. *Mater Sci Eng A* 2019, **743**:1-11.

[4] Du H, Lin X, Zheng H, *et al*. Colossal permittivity in percolative ceramic/metal dielectric composites. *J Alloys Comp* 2016, **663**:848.

[5] Naslain R. Design, preparation and properties of non-oxide CMCs for application in engines and nuclear reactors: an overview. *Compos Sci Technol* 2004, **64**:155-170.

[6] Han H, Voisin C, Guillemet-Fritsch S, *et al*. Origin of colossal permittivity in $BaTiO_3$ via broadband dielectric spectroscopy. *J Appl Phys* 2013, **113**:024102.

[7] Guillemet-Fritsch S, Valdez-Nava Z, Tenailleau C, *et al*. Colossal Permittivity in Ultrafine Grain Size $BaTiO_{3-x}$ and $Ba_{0.95}La_{0.05}TiO_{3-x}$ Materials. *Adv Mater* 2008, **20**:551.

[8] Li J, Takagi K, Terakubo N, *et al*. Electrical and Mechanical Properties of Piezoelectric Ceramic/Metal Composites in the $Pb(Zr,Ti)O_3$/Pt System. *Appl Phys Lett* 2001, **79**:2441-2443.

[9] Hwang H, Watari K, Sando M, *et al*. Low-Temperature Sintering and High-Strength

Pb(Zr,Ti)O_3-Matrix Composites Incorporating Silver Particles. *J Am Ceram Soc* 1997, **80**:791-793.

[10] Saleem M, Kim I, Song J, *et al*. Synthesis, sintering and dielectric properties of a $BaTiO_3$-Ni composite. *Ceram Int* 2014, **40**:7329-7335.

[11] Panteny S, Bowen C, Stevens R. Characterisation of barium titanate-silver composites part II: Electrical properties. *J Mater Sci* 2006, **41**:3845-3851.

[12] Ning X, Ping P, Zhou W. Large dielectric constant and maxwell effects in $BaTiO_3$/Cu composites. *J Am Ceram Soc* 2012, **95**:999-1003.

[13] Shi Z, Chen S, Fan R, *et al*. Ultra-low percolation threshold and significantly enhanced permittivity in porous metal-ceramic composites. *J Mater Chem C* 2014, **2**:6752-6757.

[14] Ortega N, Kumar A, Bhattachary P, *et al*. Impedance spectroscopy of multiferroic $PbZr_xTi_{(1-x)}O_3/CoFe_2O_4$ layered thin films. *Phys Rev B* 2008, **77**:014111.

[15] Gavalda Diaz O, Garcia L G, Liao Z, *et al*. The new challenges of machining Ceramic Matrix Composites (CMCs): Review of surface integrity. *Int J Mach Tools Manuf* 2019, **139**:24-36.

[16] Moulson A J, Herbert J M. *Electroceramics.* London: Champman and Hall, 1990

Fang G, Gao X, Zhang S, *et al*. A residual strength model for the fatigue strengthening behavior of 2D needled CMCs. *Int J Fatigue* 2015, **80**:298-305.

[17] Pecharroman C, Esteban-Betegon F, Bartolome J F, *et al*. New percolative $BaTiO_3$-Ni composites with a high and frequency independent dielectric constant (ε_r=80000). *Adv Mater* 2001, **13**:1541.

[18] Qiao L, Bi X. Dielectric behavior of $BaTiO_3$-Ni composite ferroic films. *Appl Phys A*

2009, **95**:733-738.

[19] Zhang W, Xiao Y. Mechanism of Electrocatalytically Active Precious Metal (Ni, Pd, Pt, and Ru) Complexes in the Graphene Basal Plane for ORR Applications in Novel Fuel Cells. *Energy & Fuels* 2020, **34**:2425.

[20] Li J, Chen X, Yi Z, *et al*. Broadband solar energy absorber based on monolayer molybdenum disulfide using tungsten elliptical arrays. *Mater Today Energy* 2020, **16**:100390.

[21] Lia Y, Ge X, Wang H, *et al*. Edge surface grinding of CFRP composites using rotary ultrasonic machining: comparison of two machining methods. *Int J Adv Manuf Technol* 2019, **100**:3237-3248.

[22] Cho W W, Kagomiya I, Kakimoto K I, *et al*. Paraelectric ceramics/metal dual composites $SrTiO_3$/Pt system with giant relative permittivity. *Appl Phys Lett* 2006, **89**:152905.

[23] Luo S, Yu S, Sun R, *et al*. Nano Ag-Deposited BaTiO3 Hybrid Particles as Fillers for Polymeric Dielectric Composites: Toward High Dielectric Constant and Suppressed Loss. *Appl Mater Interfaces* 2014, **6**:176.

[24] Robert P. *Analog Circuits World Class Designs.* Washington: Newnes Press 2008.

[25] Xiong Z, Cao L, High magnetic-dielectric tunability in Ni nanocrystals embedded $BaTiO_3$ films. *J Alloys Compd* 2019, **785**:200-205.

[26] Kirkpatrick S. Percolation and Conduction. *Rev Mod Phys* 1973, **45**:574.

[27] Hu L, Hecht D, Grüner G. Percolation in Transparent and Conducting Carbon Nanotube Networks. *Nano Lett* 2014, **4**:2513-2517.

[28] Sandler J, Kirk J, Kinloch I, *et al*. Ultra-low electrical percolation threshold in

carbon-nanotube-epoxy composites. *Polymer* 2003, 44:5893-5899.

[29] Zhang J L, Zheng P, Wang C L, *et al*. Dielectric dispersion of $CaCu_3Ti_4O_{12}$ ceramics at high temperatures. *Appl Phys Lett* 2005, **87**:142901.

[30] Lee S, Kang K, Han S. Low-frequency dielectric relaxation of $BaTiO_3$ thin-film capacitors. *Appl Phys Lett* 1999, **75**:1784.

[31] Levi R D, Samantaray M M, Trolier-McKinstry S, *et al*. Influence of substrate microstructure on the high field dielectric properties of $BaTiO_3$ films. *J Appl Phys* 2008, **104**:104117.

[32] Ni L, Chen X M. Dielectric relaxations and formation mechanism of giant dielectric constant step in $CaCu_3Ti_4O_{12}$ ceramics. *Appl Phys Lett* 2007, **91**:122905.

Figures

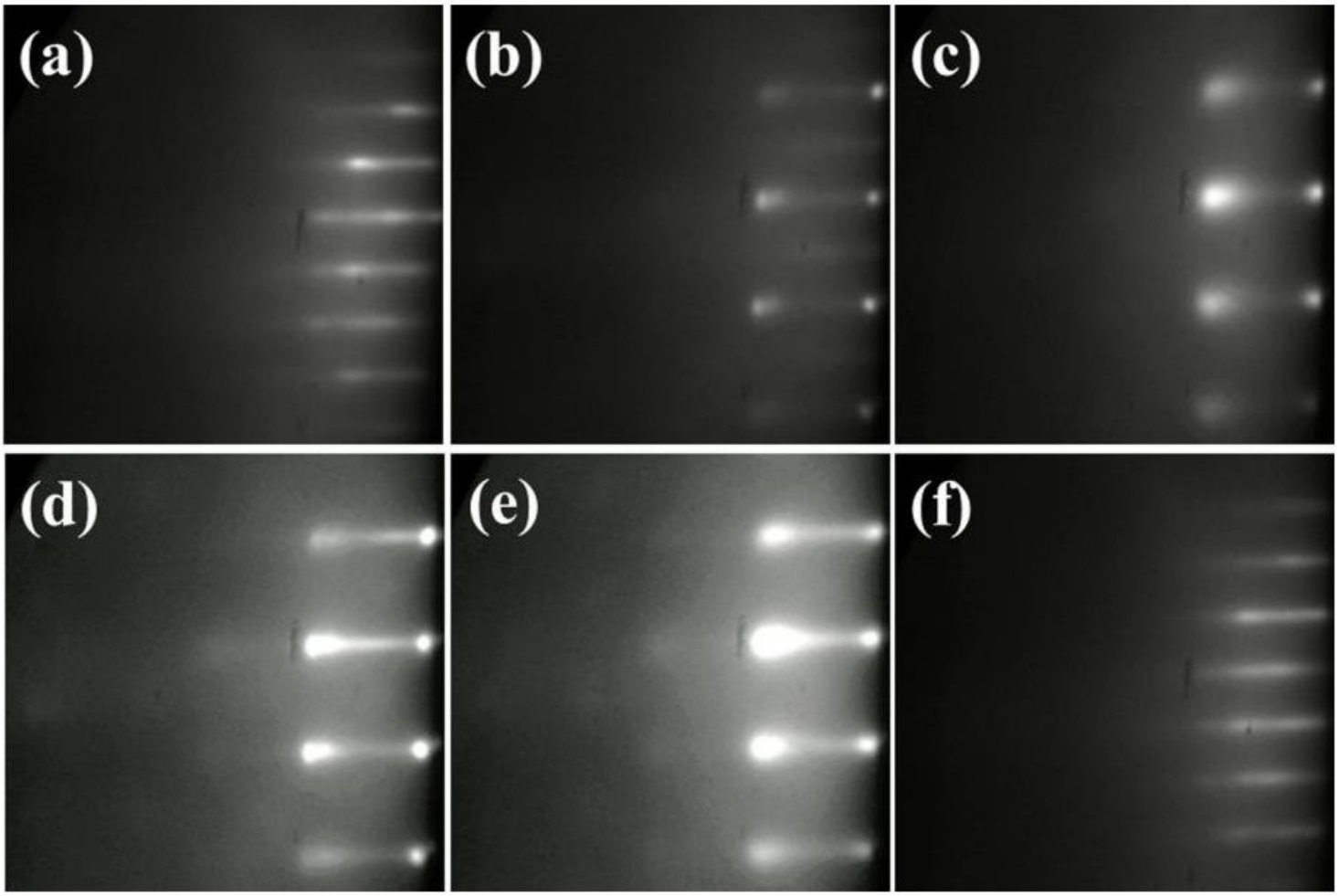

Figure 1

Evolution of RHEED patterns during the Fe NCs-BTO composites growth at various time: (a) complete surface of BTO epitaxial film deposited on (001) SrTiO3 substrates, and the Fe NCs deposition on BTO surface at (b) 50 s, (c) 100 s, (d) 250 s and (e) 400 s, (f) fresh surface of BTO grown on the Fe NCs.

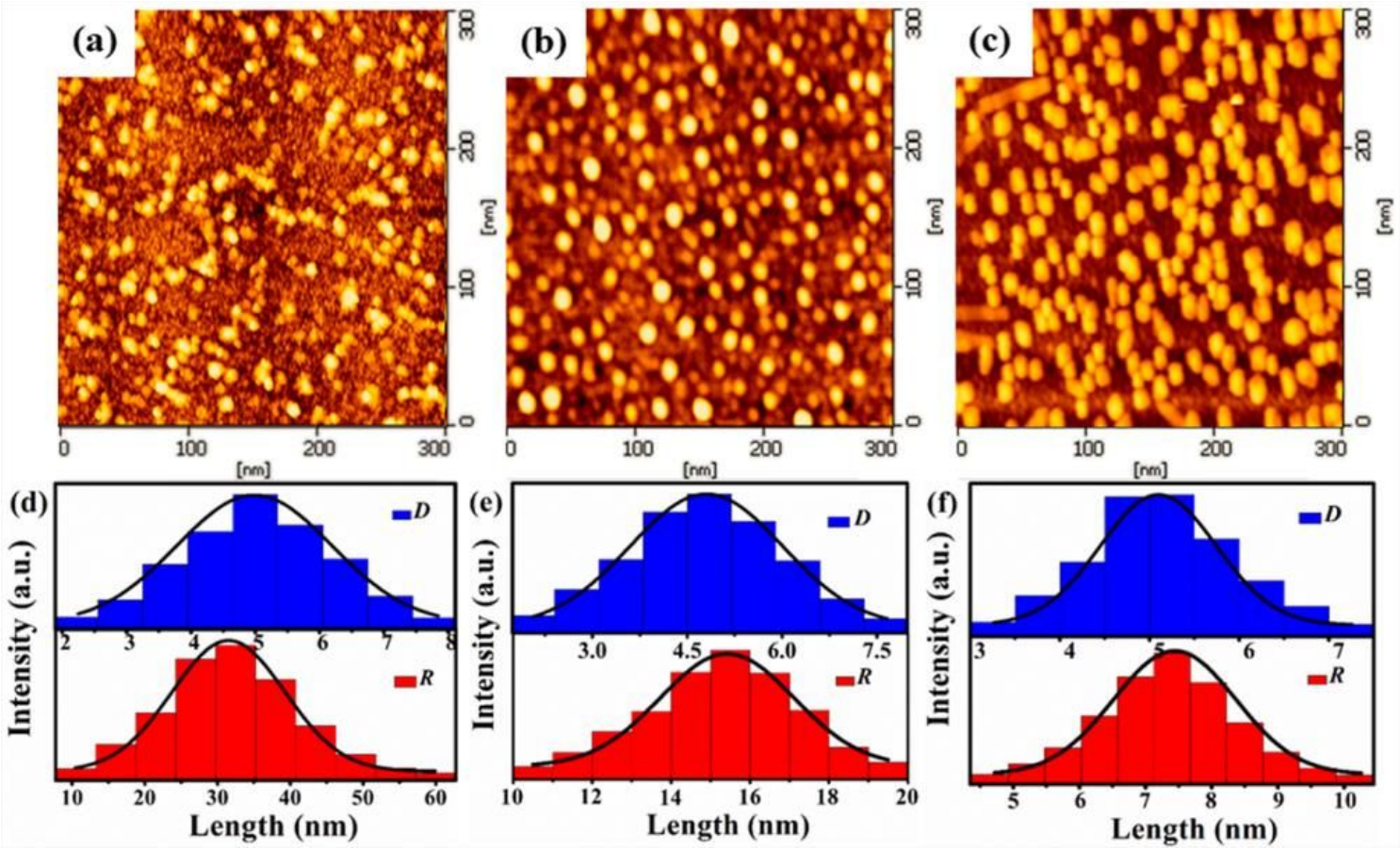

Figure 2

AFM images of (a) P1, (b) P2 and (c) P3 sample; D and R distribution of Fe NCs fitted by a log-normal distribution of (d) P1, (e) P2 and (f) P3 sample, respectively.

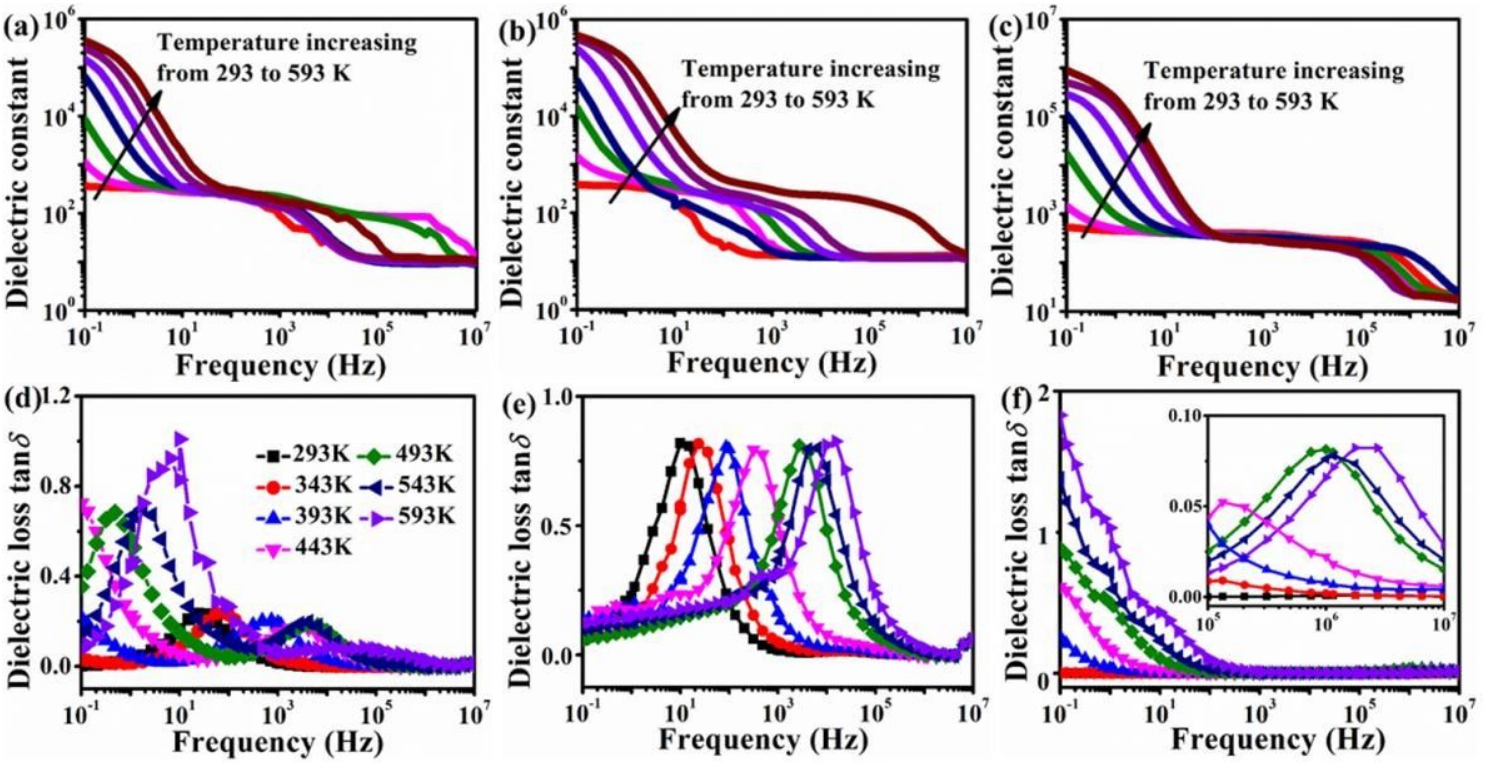

Figure 3

Dielectric constant at varied temperature of (a) P1, (b) P2 and (c) P3 sample; dielectric loss tanδ of (d) P1, (e) P2 and (f) P3 at varied temperatures. The inset of (f) is the enlarged view pattern at high frequency.

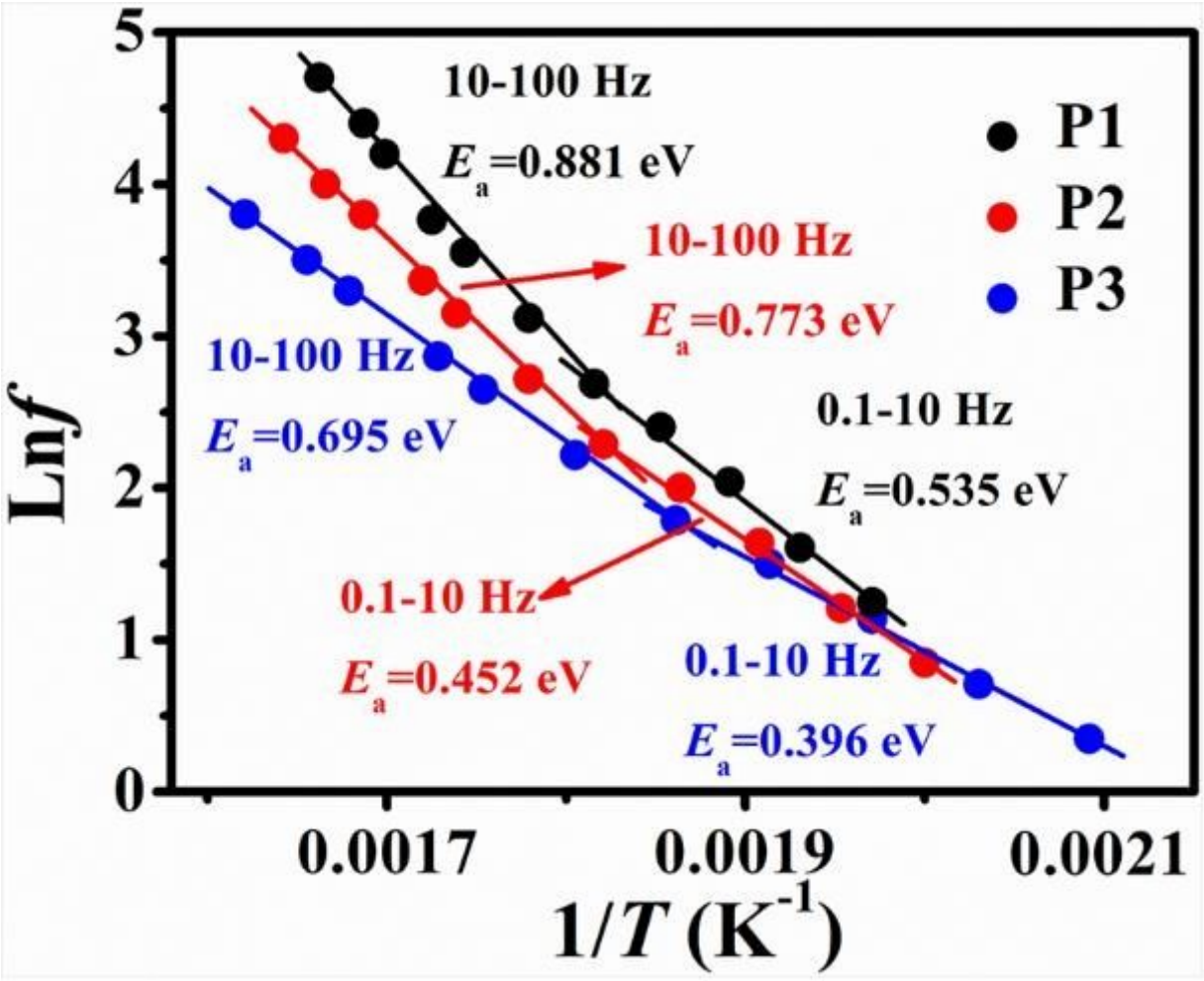

Figure 4

Activation energy of thermally activated relaxations for the samples.

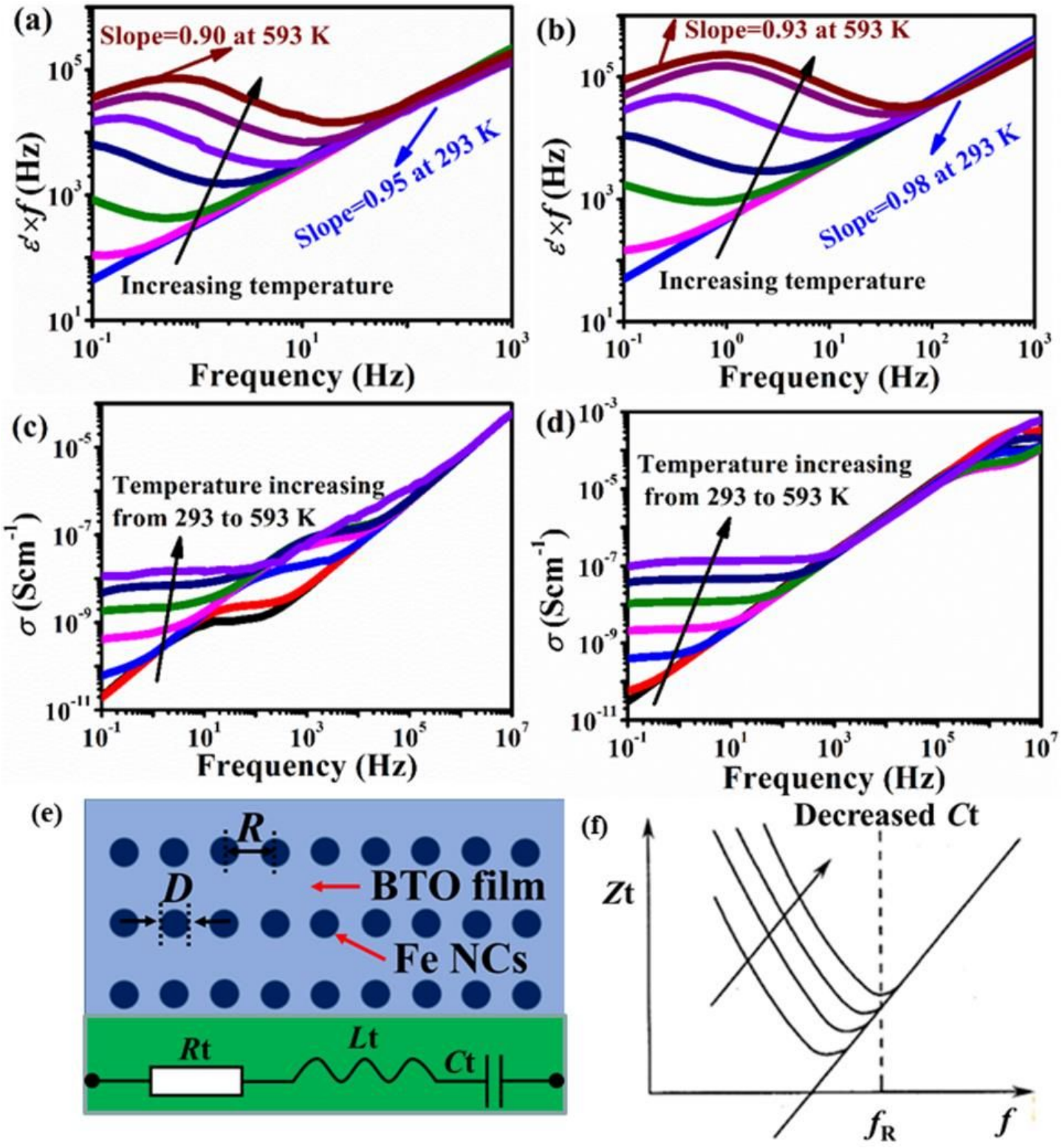

Figure 5

Lg(ε'xf) vs lgf plot of (a) P1 and (b) P3 sample at different temperatures; frequency dependence ac conductivity (σ) of varied samples at different temperature: (c) P1 and (d) P3, respectively; (e) schematic diagram and of Fe NCs-BTO composites, and the below inset displays the equivalent electric model of this system, where the Rt, Lt and Ct is the total resister, inductance and capacitance, respectively; (f) the frequency dependence total impedance (Zt) of RLC electric model.